Journal of Engineering Mathematics **46:** 127–146, 2003.

On the use of boundary-integral equation methods for unsteady free-surface flows

G. COLICCHIO and M. LANDRINI
INSEAN, The Italian Ship Model Basin, Via di Vallerano 139, 00128 Roma, Italy
(E-mail: maulan@waves.insean.it)

Received 5 June 2001; accepted in revised form 14 October 2002

Abstract. The Mixed Eulerian-Lagrangian Methods (MEL) for free-surface potential flows solved by boundary-integral equations (BIEs) is considered, and the diffusion and dispersion errors are studied in the discrete linearized problem. The diffusion error is the base for the stability analysis of the scheme; both the errors give indications on the accuracy of the numerical solution. The study is divided into two steps: comparison of the discrete dispersion relation with the analytical solution and coupling with different time-integration schemes. In particular, a stability analysis of the Runge-Kutta and Taylor-expansion schemes, previously not given in the literature, is addressed. It is shown that MEL methods based on first- and second-order explicit Runge-Kutta and Taylor-expansion schemes are unstable, regardless of the technique adopted to discretize the BIEs. Higher-order Runge-Kutta and Taylor-expansion schemes lead to conditionally stable methods. Known results for explicit, implicit and explicit-implicit Euler schemes are recovered by the present analysis. The theoretical predictions of the errors are confirmed for two different boundary-element techniques: a high-order panel method based on B-Splines to solve for the velocity potential and a spectrally-accurate method based on the Euler-McLaurin summation formula to solve directly for the velocity field.

Key words: boundary-integral equations, dispersion and diffusion errors, free-surface flows, stability of numerical schemes.

1. Introduction

An efficient numerical method for studying unsteady nonlinear inviscid free-surface flow problems is based on boundary-integral equations (BIEs). For a given configuration of the boundary domain, the velocity field is computed by suitable integral equations (Eulerian step), and the evolution of the fluid domain is determined by time-stepping based on the free-surface evolution equations. In case of a free-floating vessel, the equations of body motion have to be solved simultaneously. This approach, introduced by Longuet-Higgins and Cokelet [1] for periodic problems and, independently, by Faltinsen [2] for floating-body problems, has been proved accurate and reliable for a variety of wave and wave-body interaction problems until breaking occurs. Often, the free surface is tracked in a Lagrangian fashion, and the method is referred to as the Mixed Eulerian-Lagrangian (MEL) formulation. This name is used also when free-surface points are allowed to move only in the vertical direction, whence the method is not strictly Lagrangian. In this procedure, a great deal of attention is paid to the accurate solution of the Eulerian step using, for example, high-order panel methods (see *e.g.* [3]), as well as methods for speeding-up the numerical solution, as in [4].

Although the investigation of the stability and time-accuracy of the overall algorithm is of major relevance, it is less studied. In [5, 6], a van Neumann analysis was performed for the free-surface equations without considering the effect of spatial discretization, and stability

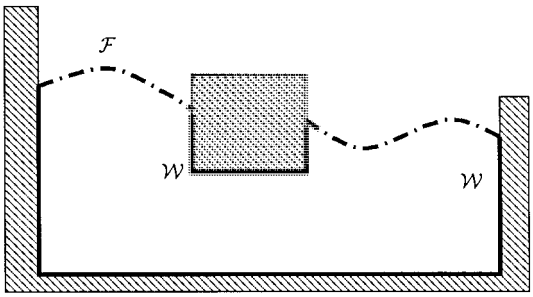

Figure 1. Illustration of free-surface flow showing the nomenclature.

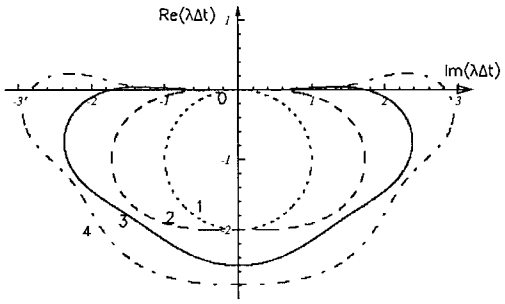

Figure 2. Stability domain of Runge-Kutta schemes of order $r = 1$ to 4. For $r = 1$, the stability boundary is a circle with unit radius.

conditions were derived. In [7] Nakos *et al.* generalized the spectral analysis and explicitly showed the effect of spatial discretization based on third-order splines. Recently, the same method has been adopted and generalized by Buchmann [8] who gave a thorough discussion of the stability properties of an algorithm based on three-dimensional B-Spline discretization. In these Fourier-type approaches, the finite extent of the fluid domain is not taken into consideration.

The matrix method introduced by Park and Thoesch [9] allows a more complete and flexible analysis. A comprehensive application of the matrix method is given in [10] for two- and three-dimensional problems using two different BIEs solvers.

In this paper, the matrix method is used to show that some stability properties of MEL methods for the linearized problem can be stated in a general way by exploiting the properties of the influence matrices, regardless of the technique adopted to solve the boundary-integral equations. The analysis is developed for explicit methods based on Runge-Kutta and Taylor-Expansion time-integration schemes, up to fourth-order accuracy. These cases have not been discussed in the literature, although they are widely used in fully-nonlinear simulations of free-surface flows. Known results for explicit- and implicit-Euler methods and for the mixed explicit-implicit Euler method, introduced in [7], are also recovered.

The general theoretical results are confirmed for two different methods. First, the higher-order panel method based on B-Splines to solve the problem in terms of the velocity potential, (see [3]), is considered. In spite of differences in the implementation, the results are in agreement with those presented by Buchmann for the three-dimensional problem. In the second method described in [4, 11, 12], one deals directly with the velocity along the fluid boundary; the stability of this approach, which has never been analyzed before, is addressed here.

2. Mathematical preliminaries

We consider the Mixed Eulerian-Lagrangian formulation (MEL) for computing the nonlinear free-surface flow of an inviscid fluid. The two-dimensional fluid domain Ω, sketched in Figure 1, is bounded by the free surface $\mathcal{F}$ and by some impermeable surfaces $\mathcal{W}$ moving with a known, possibly zero, velocity $\boldsymbol{V}$. For an inviscid fluid in irrotational motion, the flow field is described by following equations (see [1]):

$$\nabla^2\varphi = 0 \qquad \text{in } \Omega \tag{1a}$$

$$\frac{\partial\varphi}{\partial\nu} = \boldsymbol{V}\cdot\boldsymbol{v} \qquad \text{on } \mathcal{W} \tag{1b}$$

$$\frac{\mathrm{D}\boldsymbol{x}}{\mathrm{D}t} = \nabla\varphi, \quad \frac{\mathrm{D}\varphi}{\mathrm{D}t} = \frac{1}{2}|\nabla\varphi|^2 - g\eta + p_a \qquad \text{on } \mathcal{F}, \tag{1c}$$

where φ is the velocity potential, $\boldsymbol{g}$ is the acceleration-of-gravity vector, $\eta = \boldsymbol{x}\cdot\boldsymbol{e}_z$ is the vertical coordinate of $\mathcal{P}$, p_a is a known ambient pressure acting on the free surface, and $\boldsymbol{v}$ the unit vector normal to the boundary pointing outward. Equations (1c) are the kinematic and dynamic boundary conditions on the free surface in Lagrangian form, *i.e.*, following the motion of the fluid particle $\mathcal{P}$, with coordinates $\boldsymbol{x}(\mathcal{P}, t)$. The dynamic boundary condition follows from Bernoulli's equation for points on the free surface.

At a given time, t_0, the geometry of the boundary $\partial\Omega = \mathcal{F}\cup\mathcal{W}$, the potential φ along $\mathcal{F}$, and the normal gradient $\partial\varphi/\partial\nu$ on $\mathcal{W}$ are known. The solution may then be computed in time by a two-step procedure, as follows :

1. *Kinetic step* (Eulerian): The geometry is 'Frozen' and the velocity field is computed by solving a boundary-value problem for the Laplace equation:
$$\nabla^2\varphi = 0, \qquad \varphi \text{ given on } \mathcal{F}, \qquad \partial\varphi/\partial\nu \text{ given on } \mathcal{W}; \tag{2}$$
2. *Evolution step* (Lagrangian): The free-surface geometry and the free-surface potential φ are updated in time by the Lagrangian evolution equations (1c).

Step 2 requires the velocity $\nabla\varphi$ along the free surface. An efficient approach for solving the Kinetic step relies on the boundary-integral formulation of (2) involving only unknown quantities along the domain boundary. In particular, Green's third identity yields:

$$\varphi(\boldsymbol{Q}) = \int_{\partial\Omega}\left[\varphi\frac{\partial G(\boldsymbol{Q},\boldsymbol{P})}{\partial\nu_P} - \frac{\partial\varphi}{\partial\nu}G(\boldsymbol{Q},\boldsymbol{P})\right]\mathrm{d}S_P, \tag{3}$$

where $\boldsymbol{Q}$ is a point in Ω and $\boldsymbol{P}$ lies on the boundary domain $\partial\Omega$. We can write the suitable integral equations in the compact form:

$$S_{\mathcal{F}}\left(\frac{\partial\varphi}{\partial\nu}\right) + D_{\mathcal{W}}(\varphi) = D_{\mathcal{F}}(\varphi) + S_{\mathcal{W}}\left(\frac{\partial\varphi}{\partial\nu}\right), \tag{4}$$

where S and D are, respectively, boundary-integral operators for the single and double layer on $_{\mathcal{F}}$ and $_{\mathcal{W}}$. At this stage, we do not need to discuss the actual method adopted to discretize (4).

Tracking the motion of free-surface points in Step 2 requires the evaluation of velocity components. While $\partial\varphi/\partial\nu$ arises from the solution of (4), the tangential velocity component can be computed either by taking the gradient of (3), or by numerical differentiation of the potential φ along the free surface. Since the former involves higher singularity of kernels, unless a desingularized representation of the potential is used, the second option is the most widely used. A review of desingularized methods for free-surface flows is given in [13].

The integral representation (3) is not the only possible choice. Indirect methods based on double-layer potential or vorticity distributions are discussed by Baker *et al.* [14] for two-dimensional problems. In three dimensions, the numerical solution of Baker's generalized vortex method to study free-surface and interfacial flows is fully exploited by Pozrikidis [15].

Casciola and Piva [11] and Casciola and Landrini [16] presented a direct method based on the following integral representation for the velocity field $\boldsymbol{u}$,

$$\boldsymbol{u}(\boldsymbol{Q}) = \nabla_Q \int_{\partial\Omega} \boldsymbol{u} \cdot \boldsymbol{\nu} G \mathrm{d}S_P + \nabla_Q \times \int_{\partial\Omega} \boldsymbol{u} \times \boldsymbol{\nu} G \mathrm{d}S_P, \tag{5}$$

where the velocity components $\boldsymbol{u} \cdot \boldsymbol{\nu}, \boldsymbol{u} \times \boldsymbol{\nu}$ on the free surface appear explicitly. In two dimensions, the method based on (5) is equivalent to the complex boundary-value formulation of Dold and Peregrine [12, 17]. More generally, Equation (5) is a particular case of the Poincaré integral representation, which is valid for rotational non-solenoidal vector fields [18]. For two-dimensional problems, the use of a direct velocity formulation has been extended to include lifting bodies [19] and viscous-flow problems [20]. It can be seen through integration by parts that the second integral is a Biot-Savart-type integral. Thus, in principle, some of the numerical analysis presented in [15] could be adapted to the three-dimensional case. To the authors' knowledge, a direct boundary-integral formulation for the velocity has not been used previously for three-dimensional problems.

A Lagrangian description of the free surface $\boldsymbol{x}(\xi, t)$ suitable to be coupled with (5) is:

$$\frac{\mathrm{D}x}{\mathrm{D}t} = \boldsymbol{u}, \quad \frac{\mathrm{D}u_\xi}{\mathrm{D}t} = \frac{\partial}{\partial\xi}(\frac{1}{2}u_\xi^2 - g\eta), \tag{6}$$

where ξ is a Lagrangian coordinate and u_ξ is the covariant component of $\boldsymbol{u}|_{\mathcal{F}}$ along the tangential vector $\partial\boldsymbol{x}/\partial\xi$. The dynamic condition, as expressed by the second condition in (6), is derived by taking the tangential derivative $\partial/\partial\xi$ of the dynamic condition in (1c), but it can be shown that it relies only on the Euler equation, and therefore it is also applicable in the case of rotational motion.

In the following, we consider some aspects of the stability and accuracy of MEL methods when applied to solve *linearized* free-surface problems. The procedure can be applied to any boundary-integral formulations adopted within a MEL approach to solve for the Kinetic step.

3. Error analysis

3.1. PERIODIC PROBLEM

In this section, we use the matrix method introduced in [9, 10] to perform an error analysis of the linearized two-dimensional periodic problem governed by the equations:

$$\nabla^2\varphi = 0 \quad \text{in } \Omega_0, \tag{7a}$$

$$\dot{\eta} = \frac{\partial\varphi}{\partial z}, \quad \dot{\varphi} = -g\eta \quad \text{on } \mathcal{F}_0, \tag{7b}$$

where the suffix$_0$ denotes the mean configuration of the domain boundary, and the dot denotes the partial derivative with respect to time.

In the linearized problem, the horizontal motion of free-surface points is neglected, and the relevant unknowns are the wave elevation η and the potential φ at the mean free surface. In discrete form, the unknowns are represented by a vector with $2N$ components:

$$\boldsymbol{U} = \{\eta_1, \ldots, \eta_N, \varphi_1, \ldots, \varphi_N\}^T = \{\boldsymbol{\eta}, \boldsymbol{\varphi}\}^T. \tag{8}$$

By discretizing the integral equation (4), we can write the unknown boundary data $\partial\varphi/\partial\nu$ in the form

$$\mathcal{S}\left\{\frac{\partial \boldsymbol{\varphi}}{\partial \nu}|_{\mathcal{F}}\right\} = \mathcal{D}\{\varphi|_{\mathcal{F}}\} \rightarrow \left\{\frac{\partial \boldsymbol{\varphi}}{\partial \nu}|_{\mathcal{F}}\right\} = \mathcal{S}^{-1}\mathcal{D}\{\boldsymbol{\varphi}|_{\mathcal{F}}\} \rightarrow \left\{\frac{\partial \boldsymbol{\varphi}}{\partial \nu}|_{\mathcal{F}}\right\} = B\,\{\boldsymbol{\varphi}|_{\mathcal{F}}\}\,, \tag{9}$$

where the influence matrices $\mathcal{S}$ and $\mathcal{D}$ stand for the discrete counterpart of the single- and double-layer integral operators, and $B = \mathcal{S}^{-1}\mathcal{D}$. We assume that periodicity is enforced either by using the periodic form of the fundamental solution, or by mapping the domain onto a closed contour. In the case of finite depth, the no-penetration boundary condition on a flat bottom can be modeled by the method of images or by discretizing explicitly the bottom boundary. In either case, we can obtain evolution equations for the free-surface unknowns by inserting (9) in Equations (7b), *i.e.*,

$$\left\{\begin{array}{c}\dot{\boldsymbol{\eta}}\\ \dot{\boldsymbol{\varphi}}\end{array}\right\} = \left[\begin{array}{cc} 0 & B\\ -gI & 0\end{array}\right]\left\{\begin{array}{c}\boldsymbol{\eta}\\ \boldsymbol{\varphi}\end{array}\right\} = \Pi\left\{\begin{array}{c}\boldsymbol{\eta}\\ \boldsymbol{\varphi}\end{array}\right\}. \tag{10}$$

The matrix:

$$\Pi = \left[\begin{array}{cc} 0 & B\\ -gI & 0\end{array}\right]$$

embodies the (spatial) discretization of the integral equations. The properties of the discretized boundary-integral operator are given by the sub-matrix B. Equations (10) can be interpreted as a set of ordinary differential equations whose numerical solution requires the use of a time-marching scheme. The properties of the spatial discretization and time integration will be studied in the next sections.

3.1.1. *Properties of the matrices* Π *and* B

The eigenvalues λ of the matrix Π are, by definition, solutions of the equation $\det(\Pi - \lambda I) = 0$, that is,

$$\det\left(\left[\begin{array}{cc} 0 & B\\ -gI & 0\end{array}\right] - \lambda\left[\begin{array}{cc} I & 0\\ 0 & I\end{array}\right]\right) = 0 \quad \Rightarrow \quad \det\left[\begin{array}{cc} -\lambda I & B\\ -gI & -\lambda I\end{array}\right] = 0.$$

The determinant of a matrix $n \times n$ does not change when the i-th row a_{ij} is altered by the sum of a linear combination of the others $\sum_{k\in J} b_k a_{kj}$, $J = [1, \ldots, i-1] \cup [i+1, \ldots n]$. In fact, $\det A = \sum_{j=1}^{n} a_{ij}A_{ij}$, where A_{ij} is the adjoint to the element a_{ij}. If $\bar{a}_{ij} = a_{ij} + \sum_{k\in J} b_k a_{kj}$ then $\det \overline{A} = \sum_{j=1}^{n} a_{ij}A_{ij} + \sum_{k\in J} b_k \sum_{j=1}^{n} a_{kj}A_{kj}$, where $\sum_{j=1}^{n}\sum_{k\in J} b_k a_{kj}A_{kj} = 0$, because it is the determinant of a matrix with a row that is a linear combination of the others.

The matrix Π has dimensions $2N \times 2N$. By summing the i-th row multiplied by $-g/\lambda$ with the $(i+N)$-th row, we obtain:

$$\det\left[\begin{array}{cc} -\lambda I & B\\ 0 & -\lambda I - \dfrac{g}{\lambda}B\end{array}\right] = 0 \Rightarrow (-\lambda^N)\det\left(-\lambda I - \frac{g}{\lambda}B\right) = 0 \Rightarrow \det\left(\frac{\lambda^2}{g}I + B\right) = 0.$$

Therefore, if σ_i is an eigenvalue of B, we have $\lambda^2 = -g\sigma_i$, that is:

$$\lambda_{2i-1,2i} = \pm\sqrt{-g\sigma_i}. \tag{11}$$

Similarly, the eigenvectors $\{\boldsymbol{t}_1\boldsymbol{t}_2\}^T$ of the matrix Π are related to those of the sub-matrix B. By definition, we have:

$$\Pi \left\{ \begin{array}{c} \boldsymbol{t}_1 \\ \boldsymbol{t}_2 \end{array} \right\} = \lambda \left\{ \begin{array}{c} \boldsymbol{t}_1 \\ \boldsymbol{t}_2 \end{array} \right\} \quad \Rightarrow \quad \left[\begin{array}{cc} 0 & B \\ -gI & 0 \end{array} \right] \left\{ \begin{array}{c} \boldsymbol{t}_1 \\ \boldsymbol{t}_2 \end{array} \right\} = \pm\sqrt{-g\sigma} \left\{ \begin{array}{c} \boldsymbol{t}_1 \\ \boldsymbol{t}_2 \end{array} \right\},$$

that is, $B\boldsymbol{t}_2 = \pm\sqrt{-g\sigma}\boldsymbol{t}_1$ and $g\boldsymbol{t}_1 = \mp\sqrt{-g\sigma_2}\boldsymbol{t}_2$. Therefore $\boldsymbol{t}_2$ is exactly the generic eigenvector φ of B and $\boldsymbol{t}_1 = \pm\sqrt{-\sigma/g}\varphi$.

By using (9), we can eliminate $\boldsymbol{\eta}$ from (10) to get $\ddot{\boldsymbol{\varphi}} + gB\boldsymbol{\varphi} = 0$, and by projecting onto the base of eigenvectors or B, that is, $\sum_{i=1}^{N} \ddot{\varphi}_i \boldsymbol{\varphi}_i = \sum_{i=1}^{N} -g\sigma_i\varphi_i\boldsymbol{\varphi}_i$, we obtain a set of N uncoupled equations:

$$\ddot{\varphi}_i + g\sigma_i\varphi_i = 0, \tag{12}$$

which is the discrete version of the continuous equation $\ddot{\phi} + \omega^2\phi = 0$, where:

$$\phi = \frac{ga}{\omega}\frac{\cosh(k(h+z))}{\cosh(kh)}\sin(kx - \omega t), \qquad \omega^2 = gk\tanh(kh) \tag{13}$$

is the potential of the Airy wave in water of depth h, with angular frequency ω. Therefore, φ_i and $g\sigma_i$ are discrete approximations to (13) for wave number $k = i$.

From this analogy, the analysis of the eigenvalues $g\sigma_i$ of the matrix B gives a first indication of the behaviour of the error: if one of the eigenvalues is negative or complex, then the numerical scheme is not stable regardless of the time-integration algorithm adopted. In the following, the $g\sigma_i$ are assumed to be real and non-negative. It is worth stressing that the difference $\omega - \sqrt{g\sigma_i}$ gives the dispersion error induced by the spatial discretization, as will be shown later by some examples.

3.1.2. *Explicit Runge-Kutta methods*

For an r^{th}-order Runge-Kutta scheme, the discretized evolution equations (10) read:

$$\left\{ \begin{array}{c} \boldsymbol{\eta} \\ \boldsymbol{\varphi} \end{array} \right\}^{(n+1)} = \left[I + \Delta t\,\Pi + \frac{\Delta t^2}{2}\Pi^2 + \ldots + \frac{\Delta t^r}{r!}\Pi^r \right] \left\{ \begin{array}{c} \boldsymbol{\eta} \\ \boldsymbol{\varphi} \end{array} \right\}^{(n)}, \tag{14}$$

where $^{(n)}$ stands for the n-th time step. For linearized problems, Equation (14) also applies to the Taylor-expansion scheme of the same order [21].

Let us introduce the eigenvalues λ_j and the corresponding eigenvectors $\boldsymbol{u}_j$ of the matrix Π, where, by definition, $\lambda_j\boldsymbol{u}_j = \Pi\boldsymbol{u}_j$, and express the unknown vector as a linear combination of the eigenvectors $\boldsymbol{u}_j$

$$\left\{ \begin{array}{c} \boldsymbol{\eta} \\ \boldsymbol{\varphi} \end{array} \right\}^{(n)} = \sum_{j=1}^{N} a_j^{(n)}\boldsymbol{u}_j, \tag{15}$$

where the coefficients $a_j^{(n)}$ depend on time. Use of Equation (15) implies that the eigenvectors $\mathbf{u}_j$ form a complete base. Actually, Π can have equal eigenvectors for $\lambda = 0$ having the form $\{0t_2\}^T$, where t_2 is the eigenvector of B corresponding to $\sigma = 0$. The vectors completing the base in C^{2N} can he written as $\{t_2 0\}^T$ and represent a change in the mean value of the free surface without any dynamic consequence. Therefore, they are not relevant for the stability analysis and can be omitted if we assume that η has zero mean value.

The time evolution of the solution is described entirely through the evolution of the coefficients $a_j^{(n)}$, the eigenvectors $\boldsymbol{u}_j$ being determined once and for all both by the domain geometry and by the adopted discretization method. Hence, for stability, $a_j^{(n)}$ have to remain bounded for all n. By substituting Equation (15) in Equation (14), we have:

$$\sum_{j=1}^{N} a_j^{(n+1)} \boldsymbol{u}_j = \left[I + \Delta t \Pi + \frac{\Delta t^2}{2} \Pi^2 + \ldots + \frac{\Delta t^r}{r!} \Pi^r \right] \sum_{j=1}^{N} a_j^{(n)} \boldsymbol{u}_j. \tag{16}$$

Therefore, the evolution of the coefficients $a_j^{(n)}$ is governed by:

$$a_j^{(n+1)} = \underbrace{\left(1 + \lambda_j \Delta t + \frac{\lambda_j^2}{2} \Delta t^2 + \ldots + \frac{\lambda_j^r}{r!} \Delta t^r \right)}_{z_j} a_j^{(n)} = z_j a_j^{(n)} = z_j^n a_j^{(0)}, \tag{17}$$

where z_j is the shift operator (*cf.* [21, Vol. I, Chapt. 10–11]. For stability, $|a_j^{(n+1)}/a_j^{(0)}| < \infty$ as $n \to \infty$ and, therefore,

$$|z_j| = \left| 1 + \lambda_j \Delta t + \frac{\lambda_j^2}{2} \Delta t^2 + \ldots + \frac{\lambda_j^r}{r!} \Delta t^r \right| \leq 1, \tag{18}$$

where $|z_j|$ is also called diffusion error. In the complex plane $\mathfrak{Re}(\lambda \Delta t)$-$\mathfrak{Im}(\lambda \Delta t)$, stable conditions correspond to points inside the stability boundary $|z_j| = 1$ (see *e.g.* [21]), given in Figure 2 for $r = 1, \ldots, 4$. In the present context, Equation (18) shows that the stability properties of the Mixed Eulerian-Lagrangian Method are determined by: (i) the order r of the Runge-Kutta scheme, (ii) the time step Δt, and (iii) the (spatial) discretization represented by the eigenvalues λ_j of the matrix Π. More precisely, Π is affected both by the method chosen to solve the selected BIE and by the accuracy of the spatial discretization.

Further analysis is largely simplified by the result (11), *i.e.*, by observing that the eigenvalues λ_j of the matrix Π can be written in terms of the eigenvalues σ_j of the sub-matrix B, and that $g\sigma_j$ are real non-negative numbers approximating the wave frequencies ω^2 from the (linear) continuous dispersion relation for the problem considered. Hence, λ_j is either zero or purely imaginary. This key observation, with the aid of Figure 2, immediately gives some general results:

1. *First- and second-order Runge-Kutta schemes lead always to unstable methods, regardless of the adopted discretization algorithm of the integral equations. The stability domain does not intersect the imaginary axis.*

2. *Higher-order Runge-Kutta methods can be conditionally stable because purely imaginary λ_j lie within the stability domain.*

Finally, in the context of linear analysis, the explicit Runge-Kutta schemes (14) and the Taylor expansion schemes are equivalent [21], and therefore the latter shares the stability properties of the former. By using $\lambda = \pm i\omega$, we can plot the amplification factor (18) against the non-dimensional time step, $\omega \Delta t / 2\pi = \Delta t / T$ (*cf.* Figure 3). The intrinsic instability of first- and second-order schemes is clear. For third- and fourth-order schemes, if $\omega \Delta t / 2\pi$ is sufficiently small, *i.e.*, if the time step is small compared to the period of the wave considered, $|z| < 1$ and both schemes are dissipative. For larger values of the parameter $\omega \Delta t / 2\pi$, not shown in the figure, both schemes become unstable.

3.1.3. *Implicit Euler scheme*

For a first-order implicit scheme we have:

$$\begin{Bmatrix} \boldsymbol{\eta} \\ \boldsymbol{\varphi} \end{Bmatrix}^{(n)} = \begin{Bmatrix} \boldsymbol{\eta} \\ \boldsymbol{\varphi} \end{Bmatrix}^{(n+1)} - \Delta t \begin{bmatrix} 0 & B \\ -gI & 0 \end{bmatrix} \begin{Bmatrix} \boldsymbol{\eta} \\ \boldsymbol{\varphi} \end{Bmatrix}^{(n+1)} = (I - \Delta t \Pi) \begin{Bmatrix} \boldsymbol{\eta} \\ \boldsymbol{\varphi} \end{Bmatrix}^{(n+1)}.$$

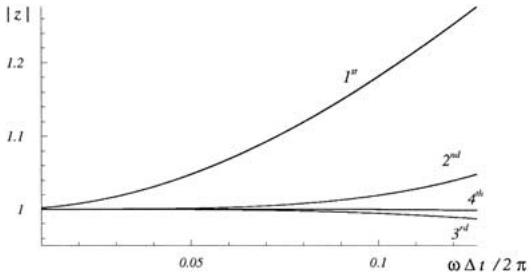

Figure 3. Amplification factor for Runge-Kutta methods, *cf.*, Equation (18).

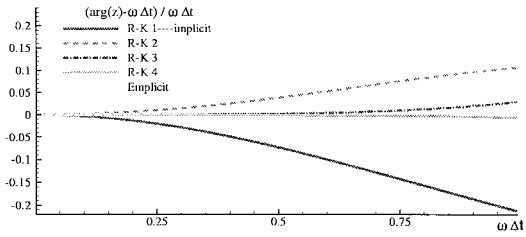

Figure 4. Dispersion error for different time-integration methods.

After some manipulations, the modulus of the shift operator can be written as:

$$|z| = |1 - \Delta t\lambda|^{-1} = \left| \frac{1}{1 \pm \sqrt{-\sigma g \Delta t^2}} \right| \leq 1, \tag{19}$$

where the latter inequality holds because $\sigma \geq 0$. Hence *the implicit Euler scheme is unconditionally stable.*

3.1.4. *Euler mixed implicit-explicit methods*

In the framework of ship-motion analysis, Nakos *et al.* [7] proposed the use of the 'Emplicit scheme', where an explicit scheme is used to obtain $\boldsymbol{\eta}$, and an implicit scheme is used for $\boldsymbol{\varphi}$. The resulting form, [10], is:

$$\begin{Bmatrix} \boldsymbol{\eta} \\ \boldsymbol{\varphi} \end{Bmatrix}^{(n+1)} = \begin{bmatrix} I & \Delta t B \\ -g\Delta t I & I - g\Delta t^2 B \end{bmatrix} \begin{Bmatrix} \boldsymbol{\eta} \\ \boldsymbol{\varphi} \end{Bmatrix}^{(n)} = F \begin{Bmatrix} \boldsymbol{\eta} \\ \boldsymbol{\varphi} \end{Bmatrix}^{(n)}. \tag{20}$$

The eigenvalues of F give the shift operators which are solutions of the equation:

$$\frac{(1-z)^2}{z} + g\Delta t^2 \sigma = 0. \tag{21}$$

Equation (21) admits complex conjugate solutions with $|z| = 1$ if $g\Delta t^2\sigma \leq 4$, otherwise the shift operators are real, and one of them is greater than one. Therefore, *the Emplicit scheme is conditionally neutrally stable*.

The last two results are already known from the literature [9]. Here, we remark that the above conclusions are not limited to a particular boundary-integral formulation or to a specific technique used to solve the integral equations.

3.1.5. *Dispersion errors*

The argument of the shift factor divided by the time step Δt gives the numerical approximation to the wave frequency ω associated with the time-integration scheme used here. Figure 4 shows the relative error on ω. As expected, as the wave frequency increases, a smaller time step is necessary to keep the dispersion error under control. This means that phase relations in a wave spectrum can be incorrect when the time step is not chosen according to the highest frequency with significant energy content when, for the total duration of the physical event. Among the first-order schemes, the implicit one is the most accurate and even better

than the second-order Runge-Kutta method; it is therefore recommended when a low-order method is required. Finally, the fourth-order Runge-Kutta scheme appears superior among those considered.

3.2. General linearized free-surface problems

The previous analysis, derived for periodic problems, can be extended to more general cases. We first consider linearized free-surface flows in a rigid tank that is forced to oscillate (*i.e.*, the 'sloshing' problem). In this case, problem (7) is completed by the no-penetration condition at the solid boundaries:

$$\frac{\partial \varphi}{\partial \nu} = \boldsymbol{V} \cdot \boldsymbol{\nu} \qquad \text{on } \mathcal{W}_0. \tag{22}$$

Now, the unknown boundary data include the potential $\varphi|_{\mathcal{W}}$ along the walls, and can be written as:

$$\left\{ \frac{\partial \boldsymbol{\varphi}}{\partial \nu}|_{\mathcal{F}} \boldsymbol{\varphi} \Big|_{\mathcal{W}} \right\}^T = \underbrace{\begin{bmatrix} B_1 & A_1 \\ B_2 & A_2 \end{bmatrix}}_{A} \left\{ \varphi|_{\mathcal{F}} \frac{\partial \boldsymbol{\varphi}}{\partial \boldsymbol{\nu}} \Big|_{\mathcal{W}} \right\}^T, \tag{23}$$

The influence matrices follow from the discretization of the boundary-integral equations. In particular, the normal gradient of the potential at the free surface is written as:

$$\left\{ \frac{\partial \boldsymbol{\varphi}}{\partial \boldsymbol{\nu}} \Big|_{\mathcal{F}} \right\} = B_1 \{\varphi|_{\mathcal{F}}\} + A_1 \left\{ \frac{\partial \boldsymbol{\varphi}}{\partial \boldsymbol{\nu}} \Big|_{\mathcal{W}} \right\}, \tag{24}$$

and the evolution equations take the form:

$$\begin{Bmatrix} \dot{\boldsymbol{\eta}} \\ \dot{\boldsymbol{\varphi}} \end{Bmatrix} = \Pi \begin{Bmatrix} \boldsymbol{\eta} \\ \boldsymbol{\varphi} \end{Bmatrix} + Q. \tag{25}$$

By writing the analogue of Equation (9) for the present case, we see that the spatial discretization of solid boundaries enters explicitly, and non-trivially, in the influence matrix A, as well as in B_1. Indeed, the solid-boundary discretization affects the stability properties. On the other hand, as already pointed out in [10], the forced motion $\partial\varphi/\partial\nu|_{\mathcal{W}}$, entirely represented by Q, affects neither the matrix Π nor the stability properties of the method considered.

We note that (11) is still valid. In particular, for the sloshing problem it can be shown that the σ_i are related to the natural frequencies of the sloshing modes (*cf.* Equation (33) in the following) and, indeed, are always positive apart from the first one which is zero. This is still true when only part of the solid boundary, or of a surface-piercing body, is forced to move, with σ representing the frequency of a generic term of the modal expansion of the solution. Hence, the stability properties obtained for the periodic free-surface problem hold in case of (linearized) wave-body problems.

3.3. Remark on the velocity formulation

The previous analysis applies to the potential-flow formulation using the integral representation (3). In case of numerical methods based on the integral representation (5) for the velocity, the linearized free-surface evolution equations are

$$\frac{\partial \eta}{\partial t} = \boldsymbol{u} \cdot \boldsymbol{e}_z, \qquad \frac{\partial u_\xi}{\partial t} = -g\frac{\partial \eta}{\partial \xi}, \tag{26}$$

and the discretized integral equation is written in the form

$$\mathcal{D}_{\mathcal{F}}(u_\zeta) = \mathcal{B}_{\mathcal{F}}(u_\xi), \tag{27}$$

where $\mathcal{B}_{\mathcal{F}}$ is a Biot-Savart-type surface-integral operator. The discretized evolution equations are:

$$\left\{ \begin{array}{c} \dot{\boldsymbol{\eta}} \\ \dot{\boldsymbol{u}}_\xi \end{array} \right\} = \left[\begin{array}{cc} 0 & B \\ -g\mathcal{D} & 0 \end{array} \right] \left\{ \begin{array}{c} \boldsymbol{\eta} \\ \boldsymbol{u}_\xi \end{array} \right\} = \Pi \left\{ \begin{array}{c} \boldsymbol{\eta} \\ \boldsymbol{u}_\xi \end{array} \right\}, \tag{28}$$

where the tangential derivative of the wave height η is expressed as the (linear) matrix operator $\mathcal{D}$, and the influence matrix B results from the discretization of the integral equation (27). Following the arguments given in Section 3.1, we find that the eigenvalues of matrix Π are still given by Equation (11), with σ representing the eigenvalues of the matrix $\mathcal{D}\mathcal{B}$.

4. Discussion

Here, we apply the analysis of Section 3 to specific cases. We consider a formulation based on Green's third identity (3) for the velocity potential, and a method based on an integral representation (5) of the velocity field. In both cases, before discussing the stability issue, we give a short description of the spatial discretization procedure adopted to solve the relevant integral equations.

4.1. A B-Splines method for the harmonic velocity

In [3], a Mixed Eulerian-Lagrangian method based on B-Splines to represent both geometry and fluid-dynamic variables is presented. The order of the B-Spline adopted to describe geometry and boundary data is an input parameter which can be freely chosen. In principle, the order of the algorithm can be arbitrarily high.

A complete description of B-Splines can be found in [22]; here, we recall a few relevant details. We consider a smooth function $f(\xi)$, defined over the interval [0,1], and introduce the B-Spline approximation of f in terms of piecewise polynomials of degree $K-1$,

$$f(\xi) \simeq \sum_{j=1}^{N_v} F_j \mathcal{N}_j(\xi). \tag{29}$$

The number $N_v = N_{\text{elem}} + K - 1$ of coefficients F_j is a function of the order K and of the number of sub-intervals N_{elem} in which [0,1] is divided. The B-Spline basis functions $\mathcal{N}_j(\xi)$ spread over K intervals, at most. In the present method, the B-Spline representation is used to fit the functions rather than to interpolate them. In general, the number of coefficients N_v differs from the number N_p of data points $f(\xi_k)$. In particular, $N_p > N_v$ and the coefficients F_j are given by an over-determined system of linear algebraic equation that is solved via a 'least-squares' technique.

It is now assumed that the domain boundary is made of a set of M continuous patches. The geometry of each patch and corresponding boundary data are approximated as:

$$\boldsymbol{P}(\xi,t) \simeq \sum_{j=1}^{N_v} \boldsymbol{P}_j(t)\mathcal{N}_j(\xi) \quad \varphi(\xi,t) \simeq \sum_{j=1}^{N_v} \Phi_j(t)\mathcal{N}_j(\xi) \quad \frac{\partial\varphi}{\partial\nu}(\xi,t) \simeq \sum_{j=1}^{N_v} \Psi_j(t)\mathcal{N}_j(\xi), \quad (30)$$

where spatial and time dependences have been separated. In (30), the same parameters (order K and number of elements N_{elem}) are used in the B-Spline approximation both for the geometry and the boundary data. Once the approximated representations (30) are known, the tangential derivatives can be evaluated analytically.

The coefficients $\Phi_j(t)$, $\Psi_j(t)$ appearing in (30) are partially unknown and have to be determined by solving integral equations of the form of Equation (4). For this purpose, the general contour integral are approximated as

$$\int_{\partial\Omega} \lambda(\boldsymbol{P})\mathcal{K}(\boldsymbol{P}^\star, \boldsymbol{P})dS_P = \bigcup_{i=1}^{M} \int_{\partial\Omega_i} \lambda(\boldsymbol{P})\mathcal{K}(\boldsymbol{P}^\star, \boldsymbol{P})dS_P \simeq \bigcup_{i=1}^{M} \sum_{j=1}^{N_v^{(i)}} \Lambda_j^{(i)} C_j^{(i)}(\boldsymbol{P}^\star). \quad (31)$$

The density λ represents either φ or $\partial\varphi/\partial\nu$, $\mathcal{K}$ is the corresponding double- or single-layer kernel, and $\Lambda_j^{(i)}$ are the coefficients of the B-Spline representation of λ for the ith patch. We recall that $\mathcal{N}_j(\xi)$ is non-zero at most in K intervals of the N_{elem} used to discretize each patch. Therefore, the integral giving the influence coefficients $C_j^{(i)}(\boldsymbol{P}^\star)$ spans a sub-interval of the patch $\partial\Omega_i$. In general, $C_j^{(i)}(\boldsymbol{P}^\star)$ cannot be determined in closed form, and we adopt numerical quadrature, as discussed in detail [3].

To carry out the stability analysis, the influence coefficients are computed and assembled to build the matrix B. According to the theoretical discussion in previous paragraphs, the eigenvalue analysis of this matrix provides information on the numerical properties of the scheme. We first consider the (linearized) periodic problem of free-surface waves in deep water. The well known analytical solution ([23, Chap. IX]) is:

$$\eta = A\cos(kx - \omega t), \quad \phi = \frac{gA}{\omega}\mathrm{e}^{ky}\sin(kx - \omega t), \quad \omega^2 = gk. \quad (32)$$

In the following, we assume a spatial periodicity 2π, with $k = 1$ the longest wave in the computational domain. The eigenvalue $\sigma_k = 1, \ldots, N_v$ of the $N_v \times N_v$ matrix B gives the numerical approximation to the frequency ω of a wave with wavenumber k (*cf.* Section 3.1.). For each k, the eigenvalue analysis returns a pair of coincident σ_k with eigenvectors corresponding to a cosine or sine wave.

Figures 5 and 6 show the effect of the discretization parameters on the numerical dispersion relation, including: the number of elements N_{elem}, the B-Spline order K, the order N_{gl} of Gauss-Legendre quadrature formula adopted to compute the influence coefficients, and the number N_{cp} of collocation points. The wavenumber k is made non-dimensional by the highest wavenumber $k_{\max} = N_{\text{elem}}/2$ accommodated by N_{elem} elements. The dispersion error $E = \omega - \omega_{\text{num}}$ due to the spatial discretization is normalized by the corresponding circular frequency $\omega_{\max} = \sqrt{gk_{\max}}$.

The numerical dispersion relation is unchanged by refining the discretization (left plot in Figure 5), and the data for increasing N_{elem} lie on the same curve. Physically, this means that the error shifts towards higher frequencies as the number of elements increases. For a given N_{elem}, the error is small for $k/k_{\max} < 0.4$, with an over-prediction of the actual frequency less than 0·2% for $k \simeq 0\cdot7k_{\max}$. After that, the error changes sign rapidly, reaching a peak of about 1·2% at 90% of the Nyquist wavenumber.

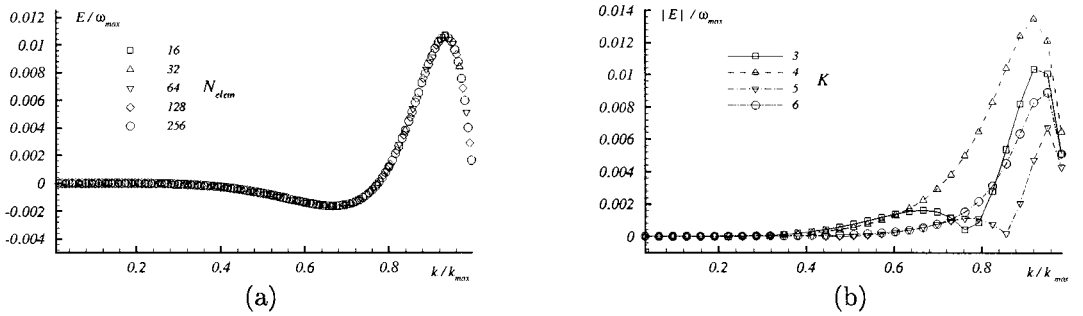

Figure 5. Deviation from the continuous dispersion relation $E = \omega - \omega_{\text{num}}$. (a) effect of the number N_{elem} of elements; in all cases, $K = 3$, $N_{\text{gl}} = 8$, $N_{\text{cp}} = 3$. (b) effect of the order K of the B-Spline; in all cases, $N_{\text{elem}} = 64$, $N_{\text{gl}} = 8$ and $N_{\text{cp}} = 3$.

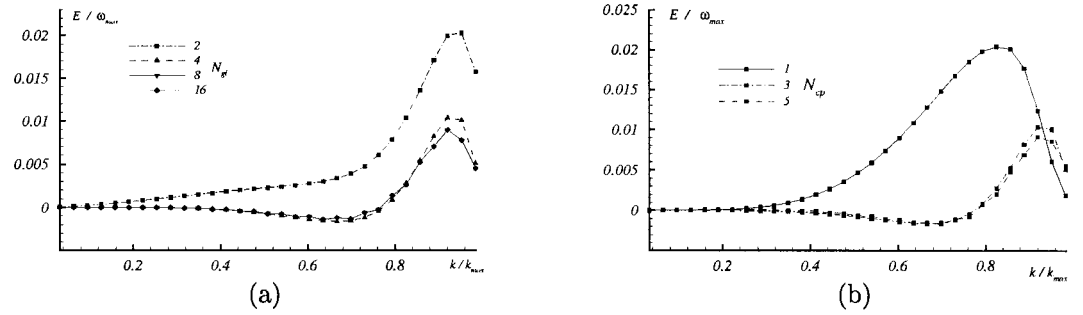

Figure 6. Deviation from the continuous dispersion relation $E = \omega - \omega_{\text{num}}$. (a) effect of the order N_{gl} of the Gauss-Legendre quadrature formula; in all cases $N_{\text{elem}} = 64$, $K = 3$, $N_{\text{cp}} = 3$. (b) effect of the number N_{cp} of collocation points; in all cases, $N_{\text{elem}} = 64$, $K = 3$, $N_{\text{gl}} = 8$.

The effect of the B-Spline order K is illustrated in of Figure 5(b), where the error is presented in absolute value. The results for $K = 3{,}4$ and $K = 5{,}6$ are superimposed for a large part of the spectrum. This is consistent with [8], where it is shown that the leading errors for the method with B-Spline of order $2n - 1$ and $2n$ are the same. In any case, $|E|$ decreases by increasing K, provided an odd or even sequence is considered, with a significant widening of the resolved spectrum, or a decrease in the error for a given cut-off frequency. Because an increase in K is accompanied by an increase of the computational effort, the previous result suggests the use of odd values of the B-Spline order.

The effect of the order of the numerical quadrature is shown in Figure 6(a). By using a two-points Gauss-Legendre formula ($N_{\text{gl}} = 2$), we observe a significantly larger error with respect to $N_{\text{gl}} = 4$, 8 and 16, which are practically superimposed. This is not surprising, because the quadrature formula needs to be of sufficiently high order compared to the B-Spline. Therefore, from a practical point of view, a gain in accuracy is achieved only by increasing wisely both K and N_{gl}.

In Figure 6(b) we see the effect of the number N_{cp} of collocation points per element. Not surprisingly, a larger number of collocation points allows for a better control of the B-Spline representation of the solution and, therefore, for a greater accuracy. On the other hand, the solution converges rapidly as N_{cp} increases (for $N_{\text{cp}} = 3$ and 5 the results are practically the same) and the algebraic system is not largely over-determined. It must be stressed that for $N_{\text{cp}} = 1$ the algebraic problem would be under-determined but, in this case, extra equations

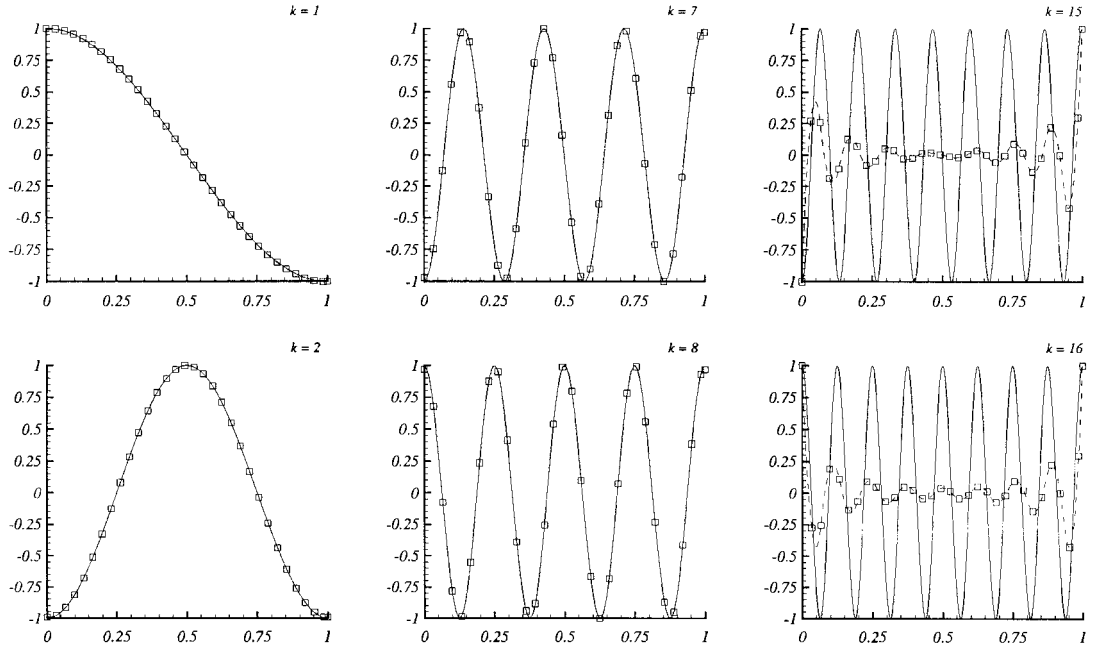

Figure 7. Natural modes for a tank with $H = L = 1$. The numerical solution obtained from the eigenvalue analysis of the influence matrix B is compared with the analytical solution, solid lines, for modes of increasing wavenumber k.

are provided by enforcing the periodicity of the B-Spline representation. No attempt has been made to check whether or not an optimum positioning of the collocation points to reduce the error exists.

Knowledge of σ_k allows us to evaluate the amplification factor z_k, and to estimate *a priori* the behavior of the numerical-solution.

We now consider finite domains and, in particular, domains bounded by solid walls. This is a common case of a wave flume or a tank. In particular, we consider a rectangular tank with beam L and depth h. The corresponding natural frequencies and natural modes are [24]:

$$\omega_k^2 = g\frac{k\pi}{L}\tanh(\frac{k\pi}{L}h), \quad \phi = \cosh(\frac{k\pi}{L}(y+h))\cos(\frac{k\pi}{L}(x+\frac{L}{2})), \quad k = 1, 2, \ldots \quad (33)$$

The eigenvalue analysis of matrix B_1 (*cf.* Equations (23–25)) provides us with approximation to expressions (33). In particular, by using N elements to disretize the free surface, we can obtain the N_v eigenvectors and eigenvalues pairs. In Figure 7 we show a comparison between analytical and numerical solutions for a tank with $H/L = 1$ and $N_v = 16$. As expected, the agreement is good for the lower-order modes, and deteriorates as the wavenumber k increases. The two highest-order eigenvectors, $N_v - 1$ and N_v, right plots, are largely in error. The uniform high-frequency oscillations are practically lost in the central part of the tank. Qualitatively, this result is not modified by refining the discretization, with the problem shifted at higher frequencies. The poor approximation of the highest-order modes is independent of the boundary-element method adopted (we performed the same analysis by a standard collocation method with linear shape function for φ and $\partial\varphi/\partial\nu$). We therefore conclude that the presence of free-surface-body intersection is the source of this error at high frequencies. The corresponding eigenvalues are largely in error with respect to the analytical values.

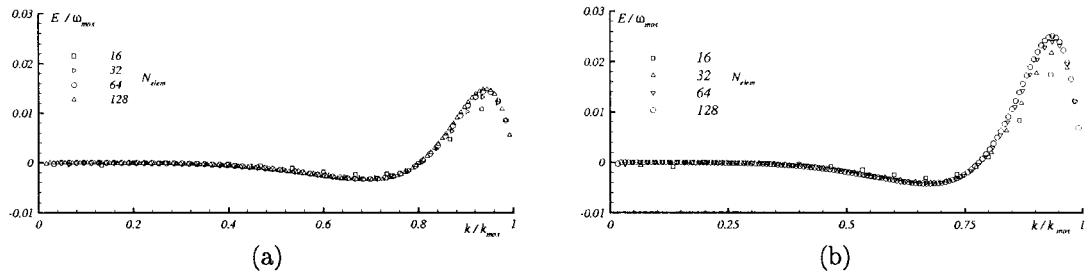

Figure 8. Deviation $E = \omega - \omega_{\text{num}}$ from the exact eigenfrequencies (33) for a tank with $H/L = 1$. For all cases, $K = 3$, $N_{\text{gl}} = 8$, $N_{\text{cp}} = 3$. (a) number N_{elem} of elements increases uniformly on the lateral walls and on the free surface. (b) number of elements on solid boundaries is kept fixed and stretching is used in proximity of the free surface. In both cases, the method of images is used to enforce the bottom boundary condition.

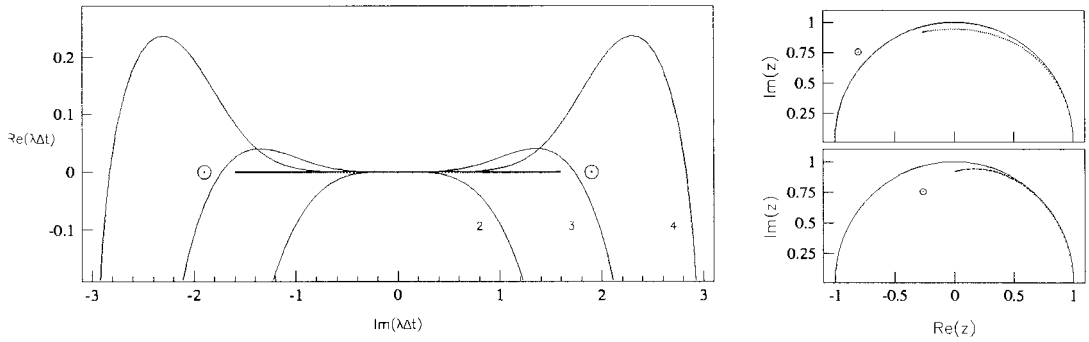

Figure 9. Stability of free-surface flows in a rectangular tank ($H/L = 0{\cdot}25$). Left: enlarged view of the stability domains of Runge-Kutta schemes (*cf.* Figure 2) and location of the eigenvalues $\lambda_j \times \Delta t$ of Π. Right: amplification factors z for third- (top half) and fourth-order (bottom half) schemes. Data are for $K = 4$, $N_{\text{elem}} = 80 \times 20 \times 20$, $\Delta t\sqrt{g/L} = 0{\cdot}2$.

In Figure 8, the numerical dispersion relation for the considered case is shown, and can be compared with the left plot of Figure 6. The error is larger only at higher frequencies, and for graphical reasons the error for the $N_v - 1$ and N_v frequencies is not reported at all. We remark that lower-order modes behave similarly to those in the periodic problem.

The effect of grading the element distribution along the lateral walls to reduce total number of elements and hence the computational effort, is also considered (*cf.* right plot in Figure 8). Differences with respect to the case with uniform distribution of the elements along the lateral walls cannot be seen for low frequencies. We observe a slightly faster growth of the error as k increases, and a larger maximum error in the highest range of wavenumbers.

For the case considered, the right diagram in Figure 9 shows the location of the amplification factors with respect to the stability circle $|z| = 1$. Results for the third- and fourth-order Runge-Kutta schemes are plotted in the top- and bottom-half parts of the figure, respectively. For the cases considered, σ_{N_v} and σ_{N_v-1} are practically the same, and the corresponding amplification factors, denoted by $\circ$, are graphically indistinguishable. In particular, in the case of the third-order scheme, z_{N_v} and z_{N_v-1} jump outside the unit circle. The left plot shows an enlarged view of Runge-Kutta stability domains and the location of eigenvalues (11) multiplied by the considered time step Δt. As discussed, all points lie on the imaginary axis. From a practical point of view, it appears to be clear that changing the time step moves these points along the imaginary axis. For the case shown, a reduction of Δt would make the third-order scheme

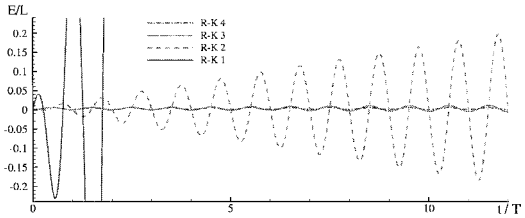

Figure 10. Linearized standing-wave problem ($H/L = 1$, $kL = 1$). Error on the height of the mid-wavelength point for Runge-Kutta methods and $\Delta t/T = 0{\cdot}001$, $K = 3$, $N_{\text{elem}} = 80 \times 50 \times 50$.

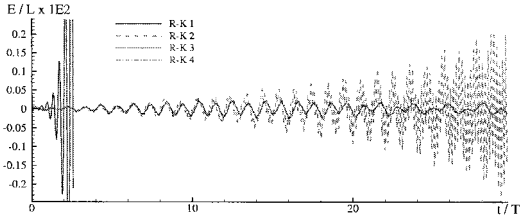

Figure 11. Linearized sloshing problem (filling level $H/L = 0{\cdot}25$, period of the sway oscillation $T\sqrt{g/L} = 2$). Error on the oscillation of the contact point for Runge-Kutta methods and $\Delta t/T = 0{\cdot}001$, $K = 3$, $N_{\text{elem}} = 80 \times 20 \times 20$.

stable. It is also confirmed that lower-order schemes are always unstable because the stability boundary is tangent to the imaginary axis.

Hereafter, the analytical solutions for the standing-wave problem and for the sloshing in rectangular tanks have been used to verify the predicted stability and dispersion errors.

A standing wave with $k = 1$ is now considered. Figure 10 shows error in the height at the mid-wavelength point. The use of first- or second-order Runge-Kutta schemes implies an amplification of the oscillating mode so that the error grows exponentially. The use of third- and fourth-order schemes leads to damped oscillations, with the error growing up to the initial amplitude of the oscillating mode. We also note that the oscillation period of the error varies according to the integration scheme considered because of the different dispersion error.

Figure 11 shows the error in the position of the contact point between the free surface and the tank wall for the sloshing problem. Both first- and second-order Runge-Kutta schemes are unstable, the error grows unbounded; for the third- and fourth-order scheme the error is bounded in time.

A similar behaviour of the error is observed in the nonlinear case. In particular, the instability of the first-order approximation is evident from the unbounded oscillation of the contact point. Also, the oscillation amplitude of the second-order approximation grows with respect to those of third- and fourth-order schemes, although the growth is slow. Figure 13 clarifies this behaviour by the free-surface profiles in a swaying rectangular tank. In the top plot, the highest-frequency mode (similar to that shown in Figure 7) is quickly amplified when a first-order scheme is used and the simulation is stopped soon after. The unstable growth for the second-order Runge-Kutta method is slower, and for $t/T = 28{\cdot}6$ both low-frequency and high-frequency modes are visible. By using higher-order schemes, we can continue the simulation indefinitely.

4.2. VELOCITY FORMULATION

We now discuss the properties of a MEL method based on the integral representation (5) for the velocity field. The implementation of the method is described in detail [4]. Multipoles-expansion and fast-summation techniques allow us to reduce the operation count to $N \log N$, where N is the number of unknowns.

Here, it suffices to give the main features of the discretization procedure. In particular, in [25] it is shown that the Poincaré formula (5) is equivalent to the Cauchy formula:

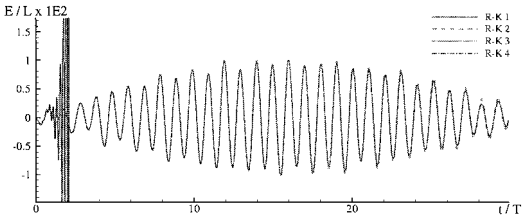

Figure 12. Nonlinear sloshing problem (filling level $H/L = 0{\cdot}25$, period of the sway oscillation $T\sqrt{g/L} = 2$), amplitude of forced sway oscillation $a/L = 0{\cdot}0069$). Evolution of the free-surface height at the contact point for Runge-Kutta methods and $\Delta t/T = 0{\cdot}001$, $K = 3$, $N_{\text{elem}} = 80 \times 20 \times 20$.

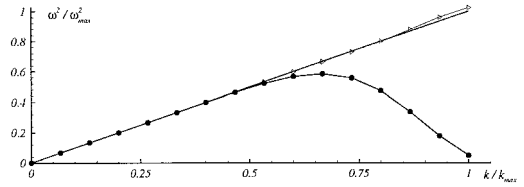

Figure 14. Numerical dispersion relation for the velocity formulation. $\omega_{\max}$ and $k_{\max}$ are the frequency and wave-number for the shortest wavelength $\lambda_{\max} = 2L/N$. The straight line gives the continuous dispersion relation which is exactly reproduced by using trigonometric polynomials. With Lagrange polynomials (•), the dispersion relation is increasingly inaccurate for $k \geq 0{\cdot}5k_{\max}$. The dispersion relation obtained using the B-Spline method (Δ) is shown too.

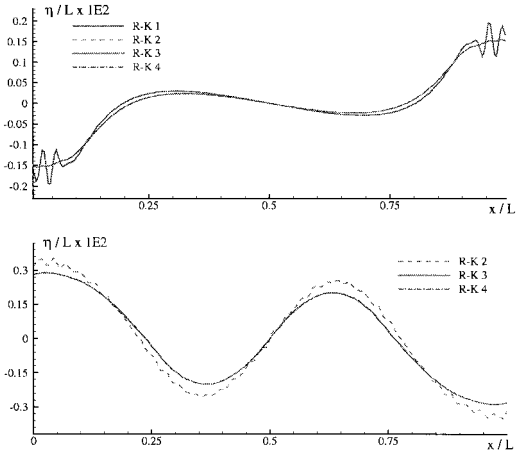

Figure 13. Nonlinear sloshing problem ($H/L = 0{\cdot}25$, oscillation period $T\sqrt{g/L} = 2$), amplitude of forced oscillation $a/L = 0{\cdot}006$). Free-surface profiles for different Runge-Kutta methods and $\Delta t/T = 0{\cdot}001$, $K = 3$, $N_{\text{elem}} = 80 \times 20 \times 20$. Top: $t/T = 0{\cdot}7$. Bottom: $t/T = 28{\cdot}6$.

$$\hat{q}(\hat{z}) = \frac{1}{2\pi \mathrm{i}} \int q \frac{\mathrm{d}z}{z - \hat{z}} \tag{34}$$

for the complex velocity $q = u - \mathrm{i}v$, and $z = x + \mathrm{i}y$. For a point $\hat{z} = z_k$ located at the boundary domain $\partial\Omega$, Equation (34) involves a Cauchy principal-value integral and can be discretized by using N points z_j distributed along $\partial\Omega$, *i.e.*,

$$qk = \sum_{\substack{j=1 \\ j \neq k}}^{N} \frac{u_{\xi,j} - \mathrm{i}u_{\zeta,j}}{z_k - z_j} \frac{\Delta\xi}{\pi \mathrm{i}} + \left\{ \frac{z_{\xi\xi}}{2z_\xi^2}(u_\xi - \mathrm{i}u_\zeta) - \frac{1}{z_\xi} \frac{\mathrm{d}(u_\xi - \mathrm{i}u_\zeta)}{\mathrm{d}\xi} \right\}_{z=z_k} \frac{\Delta\xi}{\pi \mathrm{i}}. \tag{35}$$

In (35), the boundary contour is represented as $z(\xi) = x(\xi) + \mathrm{i}y(\xi)$, ξ being a curvilinear coordinate, and z_ξ, $z_{\xi\xi}$ stand for the first- and second-order derivatives of $z(\xi)$. The points z_j are assumed uniformly distributed with spacing $\Delta\xi$; u_ξ, u_ζ are the covariant components of the velocity along the boundary. When $\partial\Omega$ is a free surface, ξ can be interpreted as a Lagrangian parameter (*cf.* Equation (6)).

For C^{2m}-continuous geometry and velocity, it can be shown [26] that the global truncation error of the Euler-McLaurin summation formula (35) is of order $\mathcal{O}(\Delta\xi^{2m})$ provided $\partial\Omega$ is a

closed smooth contour (*e.g.* for a smooth body) or the domain is periodic (*e.g.* for a spatially periodic free surface). The same behaviour holds for a compact-support velocity field on an open free surface. On physical grounds, this case can be identified with an initial-value problem on domains large enough to consider zero disturbances at the edges.

The theoretical estimate of the global truncation error assumes that the tangential derivatives in Equation (35) are known exactly. Therefore, in practice, the overall accuracy of the quadrature will depend on the ability to compute derivatives of the relevant variables. We note that, even in the linearized problem the tangential derivatives of $x(\xi)$, u_ξ and η (*cf.* Equation (26)) have to be computed, and that in the nonlinear case also the tangential derivatives of $y(\xi)$ generally differ from zero.

As expected, the numerical approximation of derivatives affects the stability properties of the overall algorithm. In fact, after some manipulations, the integral equation (27) takes the form

$$\{\mathbf{u}_\zeta\} = \underbrace{D_{\mathcal{F}}^{-1}(\tilde{B}_{\mathcal{F}} - \mathcal{D})}_{B}\{\mathbf{u}_\xi\}, \tag{36}$$

where $D_{\mathcal{F}}$ stands for the discrete version of the double-layer operator, and $\tilde{B}_{\mathcal{F}} - \mathcal{D}$ represents the discretized Biot-Savart operator, emphasizing the presence of tangential derivatives. Then, the matrix Π follows from Equation (28).

We have considered two different algorithms to approximate the derivatives: high-order Lagrange polynomials, [12], and trigonometric polynomials, [27]. The latter is preferable for its spectral convergence in case of smooth geometry and boundary data. For the periodic problem, Figure 14 shows the dispersion relation obtained by the three different procedures. In the former case, the dispersion relation is recovered with good accuracy up to $k/k_{\max} \simeq 0{\cdot}5$, with an increasingly large error for higher frequencies. For low values of k, the present result agrees with the dispersion relation computed numerically in [17]. By using trigonometric polynomials, we obtain a remarkably accurate dispersion relation over the entire range of frequenties. Moreover, the use of FFT techniques results in a more efficient code. For comparison, the best result obtained by the B-Splines method is also reported, Δ, with an accuracy that is comparable to the FFT-based version of the velocity formulation. The consequences of using the wrong dispersion relation are shown in Figure 15, where the case of a standing wave with $kL = 10$ is considered. The height of the mid-wavelength point obtained by using Lagrange polinomia shifts continuously with respect to that computed by trigonometric polynomials.

It is worth mentioning that, in both versions, the velocity formulation is more efficient than the B-Splines algorithm. On the other hand, in our experience, panel-type methods are more robust when dealing with solid boundaries meeting the free surface (*e.g.*, the case of a floating body).

5. Final remarks

The properties of the error for Mixed Eulerian-Lagrangian methods for solving linearized free-surface flows have been studied following the matrix method introduced by Troesch and his colleagues [9, 10]. In this paper, the properties of the influence matrices resulting from the discretization of boundary-integral operators are fully exploited; general results are drawn that are not limited to the specific BIEs solver adopted. MEL methods based on Euler-type schemes (implicit, explicit, emplicit) have been studied in the literature in the context of

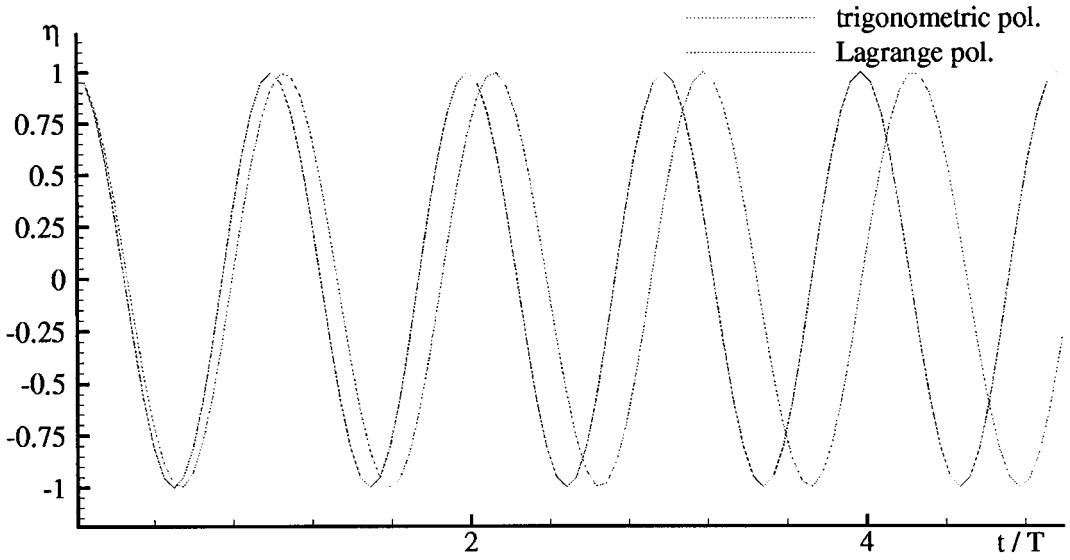

Figure 15 Linearized standing-wave problem with $kL = 10$ for the two polynomial approximations. $\Delta t/T = 0{\cdot}01$ for a fourth-order Runge-Kutta scheme, $N = 32$.

specific panel methods. Here, these results are recovered in a more general manner. Methods based on Runge-Kutta and Taylor series have not been analyzed previously. In particular, these schemes are fully equivalent within a linear analysis, and they share the same properties. First- and second-order RK schemes lead to unstable methods; eventually they are bound to fail after a finite evolution time. Third- and fourth-order schemes are conditionally stable; in these cases, the schemes are slightly dissipative and attenuation of even physical oscillations can be observed [28].

From a practical point of view, we have applied the matrix method to study the properties of rather different algorithms. The first one, introduced in [3], is based on the use of the velocity potential and the solution is represented by Green's third identity. The relevant integral equations are solved by a high-order panel method based on B-Splines to represent both the geometry and the boundary data. The influence of the discretization parameters has been discussed, and guidelines on their choice deduced. Moreover, in the case of solid-free-surface intersections, we observed that some eigenvectors of the influence matrix are largely in error with respect to the physical ones. The main feature of such numerical modes is the sharp divergent behavior near the solid boundary. We speculate that this can trigger some numerical instabilities observed in fully-nonlinear simulations of the floating-body problem, usually removed by systematic regriding of the solution near the body. The same behavior has been found in the case of a standard panel method with linear shape function, and therefore it is believed to be general.

The second MEL method analyzed is based on an integral representation of the velocity field, [11, 12], and exhibits remarkable properties in terms of stability and accuracy in recovering the continuous dispersion relation. This method is far more efficient than the panel method based on B-Splines, although its properties are not theoretically guaranteed when dealing with non-smooth-shaped boundaries, which is typical for the floating-body problem. Different than potential-flow methods, in this case tangential derivatives of some quantities enter explicitly in the discretized problem and affect the stability properties, even in the linearized case. Two

different schemes have been considered to approximate the tangential derivatives, and has been shown that trigonometric polynomials perform better than Lagrange polynomials. In practice, the difference between the two schemes is significant only for short wavelengths; for fully-nonlinear computations it is conceivable that other sources of error become more relevant (*e.g.*, saw-tooth-type instabilities). Finally, in some cases, the local character of Lagrange polynomials could be preferable to reduce the propagation of inaccuracies.

Although the present analysis is strictly valid for the linearized problem, it is reasonable to use the present results as a guideline for nonlinear simulations. To this end, we observe that several authors have adopted second-order Runge-Kutta or Taylor-expansion schemes in their work. Probably, in these cases, the time scale of the simulations was small with respect to the growth rate of the most unstable mode implied by the adopted discretization. Clearly, regridding and interpolation procedures, which are often used in nonlinear simulations, affect the (linear) theoretical growth rate of the unstable modes, if present. In any event, the present analysis does not offer an explanation of the so-called saw-tooth instability found by Longuet-Higgins and Cokelet [1]

Acknowledgement

This research has been supported by the Italian *Ministero delle Infrastrutture e Trasporti* through INSEAN Research Program 2000-2002.

References

1. M.S. Longuet-Higgins and E.D. Cokelet, The deformation of steep surface waves on water. I A numerical method of computation. *Proc. R. Soc. London* A 350 (1976) 1–26.
2. O.M. Faltinsen, Numerical solutions of transient nonlinear free-surface motion outside or inside moving bodies. In: J.V. Wehansen and N. Salvesen (eds.), *Proc. of 2*nd *Int. Conf. Num. Ship Hydr.*, Berkeley (1977) 347–357.
3. M. Landrini, G. Grytoyr and O.M. Faltinsen, A B-Spline based BEM for unsteady free-surface flows. *J. Ship Res.* 43 (1999) 1–12.
4. G. Graziani and M. Landrini, Application of multipoles expansion technique to two-dimensional nonlinear free-surface flows. *J. Ship Res.* 43 (1999) 13–24.
5. R.W. Yeung, Numerical methods in free-surface flows. *Ann. Rev. Fluid Mech.* 14 (1982) 395–442.
6. D.G. Dommermuth, D.K.P. Yue, R.J. Rapp, E.S. Chann and W.K. Melville. Deep-water plunging breakers: a comparison between potential theory and experiments. *J. Fluid Mech.* 189 (1988) 423–442.
7. D. Nakos, D.C. Kring, and P.D. Sclavounos, Rankine panel methods for transient free-surface flows. In: V.C. Patel and F. Stern (eds.), *Proc. of 6*th *Int. Conf. Num. Ship. Hydrod.*, Iowa City 1993. Washington D.C.: National Academy Press (1994) pp. 613–632.
8. B. Buchmann, Accuracy and stability of a set of free-surface time-domain boundary-element models based on B-splines. *Int. J. Num. Meth. Fluids* 33 (2000) 125–155.
9. J.H. Park and A.W. Troesch, Numerical modeling of short-time scale nonlinear waves generated by large vertical motions of non-wallsided bodies. In: *Proc. of 19th Symp. on Naval Hydrod.*, Seoul 1992. Washington D.C.: National Academy Press (1994) pp. 115–130.
10. M. Wang and A.W. Troesch, Numerical stability analysis for free-surface flows. *Int. J. Num. Meth. Fluids* 24 (1997) 893–912.
11. C.M. Casciola and R. Piva, A boundary-integral formulation for free-surface viscous and inviscid flows about submerged bodies. In: *Proc. of 5th Int. Conf. Num. Ship Hydr.*, Hiroshima (1989) A pp. 469–480.
12. J.W. Dold and D.H. Peregrine. An efficient boundary-integral method for steep unsteady water waves. In: K.W. Morton and M.J. Baines (eds.), *Numerical Methods for Fluid Dynamics II*. Oxford: Oxford University Press (1986) pp. 671–679.

13. R.F. Beck. Fully Nonlinear water wave computations using a Desingularized Euler-Lagrange time-domain approach. In: O. Mahrenholtz and M. Markiewicz (eds.), *Nonlinear Water-Wave Interaction*. Southampton (UK): WIT Press (1999) pp. 1–59.
14. G.R. Baker, D.I. Meiron, and S.A. Orszag, Generalized vortex methods for free-surface flow problems. ii: Radiating waves. *J. Sci. Comp.* 4 (1989) 237–259.
15. C. Pozrikidis, Theoretical and computational aspects of the self-induced motion of three-dimensional vortex sheets. *J. Fluid Mech.* 425 (2000) 335–366.
16. C.M. Caciola and M. Landrini, Nonlinear long waves generated by a moving pressure disturbance. *J. Fluid Mech* 325 (1996) 399–418.
17. J.W. Dold, An efficient surface-integral algorithm applied to unsteady gravity waves. *J. Comp. Phys.* 103 (1992) 90–115.
18. P. Bassanini, C.M. Casciola, M.R. Lancia and R. Piva. A boundary integral formulation for kinetic field in aerodynamics. Part I: Mathematical analysis. Part II: Applications to unsteady 2D flows. *Eur. J. Mech. B/Fluids* 10 (1991) 605–627 and 11 (1992) 69–92.
19. M. Landrini, C. Lugni and V. Bertram, Numerical simulation of the unsteady flow past a hydrofoil. *Ship Tech. Res.* 46 (1999) 14–30.
20. M. Landrini, M. Ranucci, C.M. Casciola and G. Graziani, Viscous effects in wave-body interaction. *Int. J. of Offshore and Polar Eng.* 8 (1998) 39–45.
21. C. Hirsch, *Numerical Computation of Internal and External Flows (Vol. I)* New York: John Wiley & Sons (1997) 515 pp.
22. C. de Boor, *A Practical Guide to Splines*. Heidelberg: Springer Verlag (1978) 392 pp.
23. H.N. Abramson, The dynamic behaviour of liquids in moving containers. Tech. Rep. NASA SP-106 (1966).
24. H. Lamb, *Hydrodynamics*, 6^{th} Ed. New York: Dover (1932) 738 pp.
25. M. Landrini, *Nonlinear Phenomena in Water-Waves Propagation.* PhD Dissertation Thesis in Theoretical and Applied Mechanics, Università di Roma *La Sapienza* (1993) 181 pp.
26. A. Sidi and M. Israeli, Quadrature methods for periodic singular and weakly-singular Fredholm integral equations. *J. Sci. Comp.* 3 (1988) 201–231.
27. A.J. Roberts. A stable and accurate numerical method to calculate the motion of a sharp interface between fluids. *IMA J. Appl. Math.* 31 (1983) 13–35.
28. T.S. Lundgren and N.N. Mansour, Oscillation of drops in zero gravity with weak viscous effects. *J. Fluid Mech.* 194 (1988) 479–510.